RESEARCH ARTICLE

A Codispersed Nanosystem of Silver-anchored MoS_2 Enhances Antibacterial and Antitumor Properties of Selective Laser Sintered Scaffolds

Leliang Zheng[1,2,3], Yancheng Zhong[1,2,3], Tiantian He[1,2,3], Shuping Peng[1,2,3]*, Liuyimei Yang[4]*

[1]NHC Key Laboratory of Carcinogenesis and Hunan Key Laboratory of Cancer Metabolism of Hunan Cancer Hospital and the Affiliated Cancer Hospital of Xiangya School of Medicine; School of basic Medical Science, Central South University, Changsha, Hunan 410013, China
[2]The Key Laboratory of Carcinogenesis and Cancer Invasion of the Chinese Ministry of Education, Xiangya Hospital, Central South University, Changsha, Hunan China
[3]Hunan Key Laboratory of Non Resolving Inflammation and Cancer, Disease Genome Research Center, The Third Xiangya Hospital, Central South University, Changsha, Hunan, China
[4]Ganjiang Innovation Academy, Chinese Academy of Sciences, Ganzhou 341119, China

Abstract: Tumor recurrence and bacterial infection are common problems during bone repair and reconstruction after bone tumor surgery. In this study, silver-anchored MoS_2 nanosheets (Ag@PMoS$_2$) were synthesized by *in situ* reduction, then a composite polymer scaffold (Ag@PMoS$_2$/PGA) with sustained antitumor and antibacterial activity was successfully constructed by selective laser sintering technique. In the Ag@PMoS$_2$ nanostructures, silver nanoparticles (Ag NPs) were sandwiched between adjacent MoS_2 nanosheets (MoS_2 NSs), which restrained the restacking of the MoS_2 NSs. In addition, the MoS_2 NSs acted as steric hindrance layers, which prevented the aggregation of Ag NPs. More importantly, MoS_2 NSs can provide a barrier layer for Ag NPs, hindering Ag NPs from reacting with the external solution to prevent its quick release. The results showed that Ag@PMoS$_2$/PGA scaffolds have stronger photothermal effect and antitumor function. Meanwhile, the Ag@PMoS$_2$/PGA scaffolds also demonstrated slow control of silver ion (Ag^+) release and more efficient long-term antibacterial ability. Besides, composite scaffolds have been proved to kill the MG-63 cells by inducing apoptosis and inhibit bacterial proliferation by upregulating the level of bacterial reactive oxygen species. This kind of novel bifunctional implants with antitumor and antibacterial properties provides better choice for the artificial bone transplantation after primary bone tumor resection.

Keywords: Selective laser sintering; *In situ* growth; Photothermal therapy; Apoptosis; ROS

***Correspondence to:** Shuping Peng, NHC Key Laboratory of Carcinogenesis and Hunan Key Laboratory of Cancer Metabolism of Hunan Cancer Hospital and the Affiliated Cancer Hospital of Xiangya School of Medicine; School of basic Medical Science, Central South University, Changsha, Hunan 410013, China; shuping@csu.edu.cn; Liuyimei Yang, Ganjiang Innovation Academy, Chinese Academy of Sciences, Ganzhou 341119, China; lymyang@gia.cas.cn

Received: March 14, 2022; **Accepted:** April 17, 2022; **Published Online:** June 3, 2022

Citation: Zheng L, Zhong Y, He T, *et al*., 2022, A Codispersed Nanosystem of Silver-anchored MoS_2 Enhances Antibacterial and Antitumor Properties of Selective Laser Sintered Scaffolds. *Int J Bioprint*, 8(3):577. http://doi.org/10.18063/ijb.v8i43.577

1. Introduction

Primary bone tumors such as osteosarcoma, chondrosarcoma, and Ewing's sarcoma as well as bone metastases such as lung cancer seriously threaten the survival prognosis of patients[1]. Although surgical treatment combined with chemotherapy significantly improved the survival rate of patients[2], some challenges such as tumor recurrence from post-operative tumor residue, side effects from chemotherapy, and strong ability of tumor invasion and metastasis still exist[3]. In addition, bone grafts are

required to guide new bone repair and growth in patients with bone defects after surgery operation[4,5], yet bacterial infection is a serious problem, leading to implant failure during bone reconstruction[6].

Multimodal therapies, such as photothermal therapy/photodynamic therapy (PTT/PDT), chemo-PTT, and PDT/chemotherapy therapy, make it possible to cure tumor recurrence and bacterial infection[7]. A study by Li *et al*. designed a multifunctional scaffold consisting of porous Ti6Al4V, chitosan, and selenium-doped hydroxyapatite nanoparticles[8] promoted osteoblast proliferation while inhibited tumor cells growth and bacterial viability, which can be potentially used for treating bone defects resulted from surgical resection of osteosarcoma. Some researchers have introduced photothermal agents and drugs into stents to achieve the synergistic treatment of PTT/PDT. For example, Wang *et al*. reported highly active single-atomic iron catalyst modified three-dimensional (3D)-printed bioactive glass scaffold with the ability to generate reactive oxygen species (ROS) and absorb near-infrared (NIR) laser, which can be used for antibacterial and antitumor treatment of osteosarcoma[9]. NIR laser-induced heating can also enhance the sensitivity of bacteria to antibiotics, leading to reduced drug dosage and improved treatment efficacy[10]. However, multidrug resistance of bacteria and inadequate mechanical properties of scaffolds limit their application in bone replacement materials.

MoS_2 nanosheets (MoS_2 NSs) belong to a novel type of nanomaterial with large specific surface area, easy surface modification, and high NIR photothermal conversion efficiency, which are being developed for cancer diagnosis and treatment[11-13]. Chen *et al*. developed a novel MoS_2/Bi2S3 nanomaterial based on MoS_2, which can be used for photoacoustic and computed tomography imaging and tumor photothermal therapy[14]. Cai *et al*. developed an DOX@Apt-PEG-PDA-MoS_2 nanoplatform based on MoS_2 and adaptor functionalization, which can effectively target breast cancer and cooperate with photothermal therapy[15]. Meanwhile, silver and silver-based compounds are recognized as powerful antibacterial agents due to their high bactericidal efficiency, wide bactericidal spectrum, and no bacterial resistance[5]. Silver nanoparticles (Ag NPs) not only release silver ion (Ag^+) to destroy the protein structure of bacterial cell membrane, inhibit the activities of respiratory enzymes and proteins, inhibit DNA transcription and translation, but also upregulate the level of ROS, causing oxidative damage to bacteria[16]. Hence, the combination of MoS_2 and silver may be a promising antitumor and antibacterial strategy. However, MoS_2 NSs and Ag NPs tend to agglomerate in the polymer matrix because of their large van der Waals forces, as well as the explosive release of Ag^+ is still a problem in the application of Ag-based antibacterial materials[17].

In situ growth of nanoparticles on the carrier is an effective way to solve this problem[18-21]. For example, Ali *et al*. synthesized Au@graphene mixed aerogel by *in situ* reduction using NIR radiation, in which gold nanoparticles were uniformly dispersed and enhanced the conductivity of graphene oxide (GO)[22]. Nanometer system of *in situ* growth of silver has been developed, Xu *et al*. synthesized a silver modified hollow silicon dioxide (SiO_2) nanoparticles, which showed good dispersity in ethanol and water, and had good antibacterial activity against *Escherichia coli* and *Staphylococcus aureus*[23]. However, the conditions for surface functionalization of nanomaterials are often complex and difficult to control. In general, redox reaction is an effective method to obtain Ag NPs on nanocarriers[24]. Polydopamine stands out among reducing agents because of its good biocompatibility and adhesion properties, as well as its large amount of catechol and amine groups[25]. More importantly, its catechin group can be adsorbed to nanocarriers by coordination reaction and then reduced to Ag NPs by redox reaction[26], which helps to control the content and size of Ag NPs by the concentration of Ag^+.

In this study, a codispersed Ag@$PMoS_2$ nanosystem was developed by *in situ* reduction of Ag NPs on MoS_2 NSs with polydopamine. In the Ag@$PMoS_2$, Ag NPs and MoS_2 NSs are separated from each other, where MoS_2 NSs loaded Ag NPs, while Ag NPs acts as steric hindrance to prevent the accumulation of MoS_2 NSs (**Figure 1I**). Then, Ag@$PMoS_2$ was mixed with polyglycolic acid (PGA). Finally, the composite scaffold was developed by selective laser sintering (SLS) technology (**Figure 1II**). The morphology and structure as well as the chemical composition of Ag@$PMoS_2$ were analyzed. Furthermore, the comprehensive performance of 3D scaffolds was evaluated, including photothermal performance and photothermal stability,

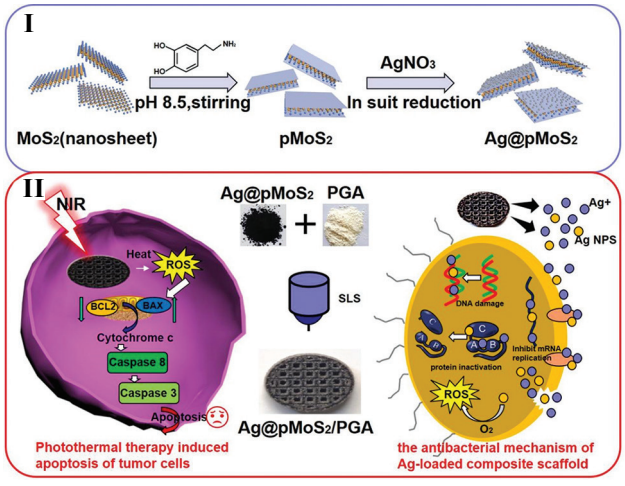

Figure 1. Schematic diagram of preparation and antibacterial and antitumor function of multifunctional scaffold. (I) Preparation process of *in situ* growth of Ag NPs on MoS_2. (II) Mechanism of antibacterial and antitumor of multifunctional therapy.

Please cite this article as: Zheng L, Zhong Y, He T, *et al*., 2022, A Codispersed Nanosystem of Silver-anchored MoS_2 Enhances Antibacterial and Antitumor Properties of Selective Laser Sintered Scaffolds, *Int J Bioprint*, 8(3):0025. http://doi.org/10.18063/ijb.v8i3.0025

antitumor and antibacterial ability, and Ag^+ release spectrum. Besides, we explored the potential mechanisms of antitumor and antibacterial stents (**Figure 1II**).

2. Experimental methods

2.1. Materials

PGA was supplied by from Shenzhen Polymtek Biomaterial Co. Ltd. (Shenzhen, China). The average molecular weight of PGA was 100 kDa. MoS_2 NSs were supplied by Nanjing XFNano Materials Tech Co. Ltd. (Jiangsu, China), with diameter in the range of 0.2 – 5 μm and more than 90% monolayer rate. Silver nitrate ($AgNO_3$) was purchased from Sinopharm Chemical Reagent Co., Ltd. Tris-HCl and dopamine hydrochloride as well as other reagents of analytical grade were purchased from Sigma (Shanghai, China). All the above raw materials were used as received.

2.2. Preparation of $Ag@PMoS_2$ nanosheets

Figure 1I shows the preparation of silver by *in situ* reduction on MoS_2 NSs. In general, 0.04 g MoS_2 NSs was added to 100 mL TRIS-HCl buffer (10 mM, pH = 8.5) and ultrasonic stirred for 2 h. Then, 0.2 g dopamine hydrochloride was added and stirred vigorously at room temperature for 12 h. Black precipitate was separated and collected at 6000 rpm for 10 min, and washed with anhydrous ethanol for 5 times. To generate Ag NPs *in situ* on PDA surface, the products obtained in the above experiments were dispersed into 100 mL ethanol under ultrasonic conditions, then 2 mL 0.12 M $AgNO_3$ solution was added into the reaction system. After mixing well and standing for 24 h, the supernatant was removed and the precipitate was resuspended with 100 mL ethanol. The mixture was added to a 250 mL oil bath and stirred with magnetic force. When the temperature rose to 80°C, 30 mL $NaH_2PO_2 \cdot H_2O$ (14.8 mg/mL) ethanol solution was added to the above mixture, reacting for 20 min. Then, the products were cooled at room temperature for 12 h and washed 6 times with anhydrous ethanol. Finally, the products were dried in a vacuum oven at 60°C for 24 h.

2.3. Scaffold preparation

As we know, PGA is a kind of non-toxic and non-immunogenicity biomaterial with excellent biodegradability and biocompatibility, which has been approved by the Food and Drug Administration for human clinical applications. Herein, PGA was used as the matrix material to prepare the composite scaffold. Specifically, the 0.1 g nanometer sample and 9.9 g PGA powder were dispersed into a beaker containing 30 mL anhydrous ethanol for ultrasonic stirring for 30 min. The composite powder was then obtained through filtering, drying, grinding, and other processes. Finally, the self-developed SLS system was used to build the 3D scaffold layer by layer. SLS could meet the personalized needs of bone implantation due to the controllable external shape and pore size of the scaffold[27-32]. Typically, a layer of 0.1 mm thick powder were spread by the roller at a constant speed; then, the powders were selectively fused by the laser beam under the control of the programmed pattern; subsequently, the powder bed was lowered by 0.1 mm and the powder was respread, the sintering process was repeated until the scaffold was complete; the primary processing parameters of the scaffold preparation were hatch distance (0.1 mm), laser power (2.7 W), and scan speed (300 mm/s). The sintered scaffold of pure PGA powder was named PGA, the sintered scaffold was named MoS_2/PGA, $PMoS_2$/PGA, and $Ag@PMoS_2$/PGA after mixing MoS_2, $PMoS_2$, and $Ag@PMoS_2$ NSs with PGA powder, respectively.

2.4. Analysis and characterization

The morphology of $Ag@PMoS_2$, $PMoS_2$, and MoS_2 was observed by transmission electron microscopic (TEM) (Morgagni 268D, FEI, USA). The chemical structure of $Ag@PMoS_2$, $PMoS_2$, and MoS_2 was analyzed by Fourier-transform infrared spectroscopy. The morphology and elemental composition distribution of $Ag@PMoS_2$, $PMoS_2$, and MoS_2 and composite scaffolds were observed by scanning electron microscopy (SEM) (EVO LS10, Zeiss, Germany) equipped with energy-dispersive spectroscopy (EDS) (XFlash 6130, Bruker, Germany). The chemical composition of $Ag@PMoS_2$, $PMoS_2$, and MoS_2 was evaluated by X-ray photoelectron spectroscopy (XPS) (ESCALAB 250, Thermo Scientific, UK). The crystal structure of $Ag@PMoS_2$, $PMoS_2$, and MoS_2 was observed by X-ray diffractometer (XRD) (Empyrean-100, PANalytical, Netherlands). The Ag^+ release spectrum of composite scaffolds in deionized water was quantitative analyzed by inductively coupled plasma optical emission spectrometer (Optima 8300, Perkin Elmer, USA).

2.5. Photothermal performance and photothermal stability of composite scaffolds

The prepared scaffolds were immersed in pure water, and the PGA, MoS_2/PGA, $PMoS_2$/PGA, and $Ag@PMoS_2$/PGA scaffolds were irradiated by a NIR laser generator. We designed pure water as the background group because water can absorb a certain amount of NIR energy[33]. Under the same laser power density (1 W/cm^2), the composite scaffold was irradiated with 808 nm laser for about 750 s, and the corresponding solution temperature data were recorded in real time to evaluate the photothermal performance of the composite scaffolds. In addition, the photothermal stability of the $Ag@PMoS_2$/PGA scaffold was evaluated by four switching cycles under NIR irradiation.

Please cite this article as: Zheng L, Zhong Y, He T, *et al*., 2022, A Codispersed Nanosystem of Silver-anchored MoS_2 Enhances Antibacterial and Antitumor Properties of Selective Laser Sintered Scaffolds, *Int J Bioprint*, 8(3):0025. http://doi.org/10.18063/ijb.v8i3.0025

2.6. Photothermal effect of scaffold to MG63 and bone marrow mesenchymal stem cell (BMSC) cells

The composite scaffolds were sterilized with 75% alcohol for 1 h and then ultraviolet for 2 h. human osteosarcoma cells (MG63) and mouse BMSC were cultured with DMEM (10% fetal bovine serum, 1% penicillin, and streptomycin) in a cell incubator (5% CO_2, 37°C) for 48 h. The cell suspensions were then placed into a composite scaffold and irradiated with or without 808 nm NIR laser for 10 min. Cell Counting Kit-8 reagent was added to each hole and incubate at 37°C for 2 h. Cell survival was evaluated by measuring the absorbance of the supernatant at 450 nm (Beckman, USA). Propidium iodide (PI) and calcein-AM were added, respectively, and the cells live/dead assay was evaluated using a fluorescence microscope (BX60, Olympus, Japan). Apoptosis rate was evaluated according to the instructions of the VFITC/PI Apoptosis Detection Kit (BIOBOX, China). For Western blotting detection of Bcl-2 and Bax expression, the MG63 cells were cocultured with the composite scaffold, then irradiated with or without 808 nm NIR laser (1 W/cm^2) for 20 min and then incubated for 2 h. Then, the protein was collected and the protein concentration was measured. Finally, the expression of Bcl-2 and Bax was examined by Western blotting.

2.7. Antibacterial function of scaffolds

The antibacterial performance of scaffolds was evaluated with Gram-negative bacteria *E. coli*. The composite scaffolds were sterilized with 75% alcohol for 1 h and then ultraviolet for 2 h. *E. coli* suspension (1 × 10^6 CFU/mL) was cultured with sterilized scaffolds and irradiated with or without 808 nm NIR for 10 min at 4 h intervals. After 24 h, the absorbance of the suspension at 600 nm was measured to evaluate the antibacterial activity of the scaffold (Beckman, USA). At the same time, the suspension was imaged by digital camera. Finally, the scaffolds attached with bacteria were fixed with 2.5% glutaraldehyde for 1 h after washed with PBS, then dehydrated in a gradient concentration of ethanol (10, 30, 50, 75, 95, and 100% v/v) for 10 min. The number and morphology of bacteria on the scaffold were observed by SEM. 2',7'-dichlorofluorescin diacetate (DCFH-DA) was used to evaluate the ROS in *E. coli*. In details, *E. coli* suspension (1 × 10^6 CFU/mL) was cultured with sterilized scaffolds and irradiated with or without 808 nm NIR for 10 min at 4 h intervals. After 24 h, *E. coli* was collected, 500 μL phosphate-buffered PBS with 10 μM of DCFH-DA was added and then incubated at 37°C for 30 min in the dark. The images were captured with fluorescence microscope (BX60, Olympus, Japan).

2.8. Statistical analysis

In this study, multiple replicate tests were performed for each group of samples and the final experimental results were expressed as mean ± standard deviation. All experimental data were statistically analyzed by SPSS software (ver. 23.0; IBM Corporation, NY, USA). The results were regarded as statistically significant only when $P < 0.05$.

3. Results and discussion

3.1. Micromorphology of MoS_2 and Ag@$PMoS_2$

Micromorphology and elemental compositions of the MoS_2 and Ag@$PMoS_2$ NSs were observed by TEM and SEM equipped with EDS. As shown in **Figure 2A**, the unmodified MoS_2 NSs presented a relative smooth surface. **Figure 2B** shows the TEM images of Ag@$PMoS_2$ NSs. It can be seen that the size of Ag particles ranges from 5 nm to 20 nm and is evenly distributed on the surface of $PMoS_2$ NSs. This is because MoS_2 is coated by PDA and has abundant phenols and nitrogenous groups on its surface, which can absorb Ag^+ and help the formation of Ag NPs[34]. The high-resolution TEM image of Ag@$PMoS_2$ nanosheets shows crystal structure with lattice spacing about 0.27 nm for the (100) plane of MoS_2 NSs and 0.237 nm for the (111) plane of metallic Ag (**Figure 2C-E**)[35,36]. In the selected area of electron diffraction images (**Figure 2F**), the lattices of (200), (111), (220), and (311) were observed, which further confirmed the formation of Ag NPs. To check the distribution of silver in $PMoS_2$ NSs, EDS assay was performed. As shown in **Figure 2G**, the silver element is uniformly distributed on the surface of $PMoS_2$ NSs. Above results indicate that the Ag^+ had been reduced to Ag NPs and distributed uniformly on the surface of $PMoS_2$ NSs, which could help with the dispersion on each other. On the one hand, the accumulation of MoS_2 NSs may be inhibited by the sandwiched Ag NPs. On the other hand, the aggregation of Ag NPs may be hindered by the MoS_2 nanosheets.

3.2. Characterization of Ag@$PMoS_2$

XRD and XPS were performed to characterize the crystal structure and chemical component of MoS_2 NSs, $PMoS_2$ NSs, and Ag@$PMoS_2$ NSs. As shown in **Figure 3A**, the pattern of the Ag@$PMoS_2$ exhibited all diffraction peaks associated to Ag and MoS_2. The diffraction peak near 14° reduces in $PMoS_2$ NSs and Ag@$PMoS_2$ NSs due to the stack of MoS_2 layers is disrupted by the PDA coating[35]. Compared with $PMoS_2$ and MoS_2, it can be observed that four new diffraction peaks at 38.13°, 44.35°, 64.52°, and 77.44° in Ag@$PMoS_2$, which belong to the (111), (200), (220), and (311) reflection planes of metallic Ag,

Please cite this article as: Zheng L, Zhong Y, He T, *et al*., 2022, A Codispersed Nanosystem of Silver-anchored MoS_2 Enhances Antibacterial and Antitumor Properties of Selective Laser Sintered Scaffolds, *Int J Bioprint*, 8(3):0025. http://doi.org/10.18063/ijb.v8i3.0025

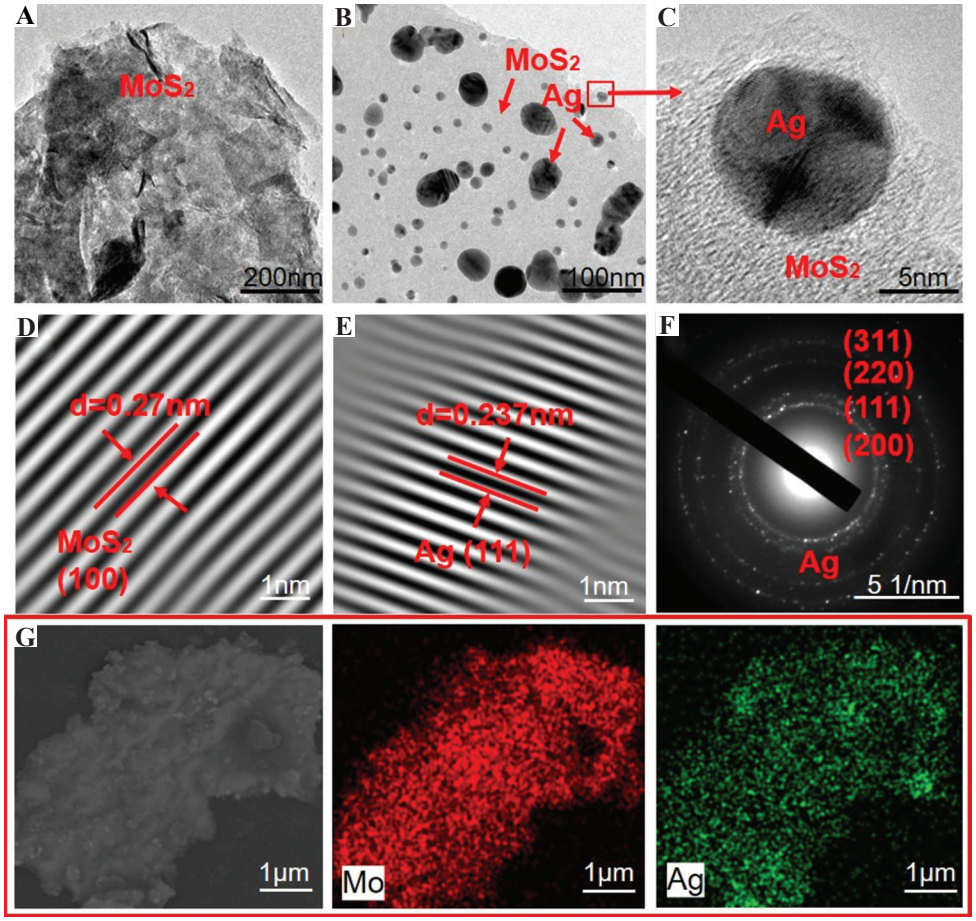

Figure 2. Micromorphology of Ag@PMoS$_2$. (A) TEM images of MoS$_2$, (B-F) TEM images of Ag@PMoS$_2$. (G) SEM images and EDS analyze of Ag@PMoS$_2$.

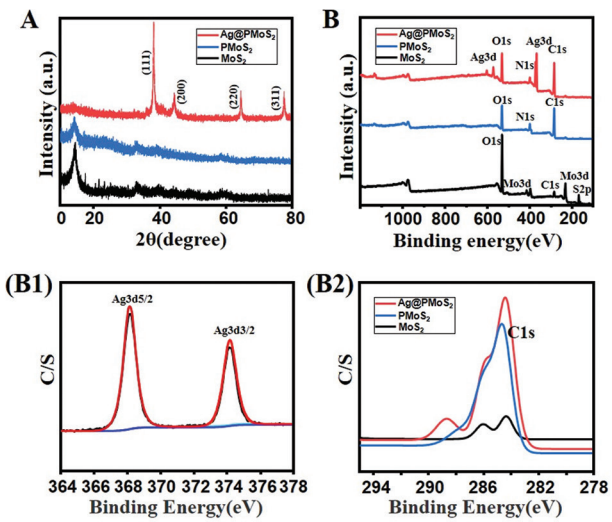

Figure 3. Characterization of Ag@PMoS$_2$. XRD (A) and XPS (B) spectra of MoS$_2$, PMoS$_2$, and Ag@PMoS$_2$. (B1) XPS for Ag3d orbits of metallic Ag@PMoS$_2$. (B2) C1s for the samples of MoS$_2$, PMoS$_2$, and Ag@PMoS$_2$.

respectively[37]. The surface elemental configurations of MoS$_2$ NSs, PMoS$_2$ NSs, and Ag@PMoS$_2$ NSs were performed by XPS. As shown in **Figure 3B**, the C, N, O, Mo, and Ag elements were detected in Ag@PMoS$_2$, in which N and C were assigned to polydopamine. Clearly, the spectrum of Ag@PMoS$_2$ appeared several new peaks was occurred at 375 – 385 and 578 – 613 eV compared to PMoS$_2$ and MoS$_2$, which were belong to Ag 3d and Ag 3p peaks of metallic Ag, respectively. **Figure 3B1** shows that at 368.1eV and 374.0eV, Ag3d nuclear horizontal spectrum can be divided into two peaks corresponding to Ag3d5/2 and Ag3d3/2 of metallic Ag, respectively[38]. As can be seen from **Figure 3B2**, the peak relative strength of Ag@PMoS$_2$ at about 298 eV is significantly higher than MoS$_2$ and PMoS$_2$, which can be attributed to the C=O band of PDA. It can be inferred that the Ag^+ could oxidize the -C-OH of polydopamine to –C=O, and the metallic Ag can be immobilized on the surface of PMoS$_2$ by the structure of quinone[39].

3.3. Microstructure and photothermal performance of scaffolds

The digital photos of PGA, MoS$_2$/PGA, PMoS$_2$/PGA, and Ag@PMoS$_2$/PGA scaffolds fabricated by SLS technology are shown in **Figure 4A-D**, respectively.

Please cite this article as: Zheng L, Zhong Y, He T, *et al*., 2022, A Codispersed Nanosystem of Silver-anchored MoS$_2$ Enhances Antibacterial and Antitumor Properties of Selective Laser Sintered Scaffolds, *Int J Bioprint*, 8(3):0025. http://doi.org/10.18063/ijb.v8i3.0025

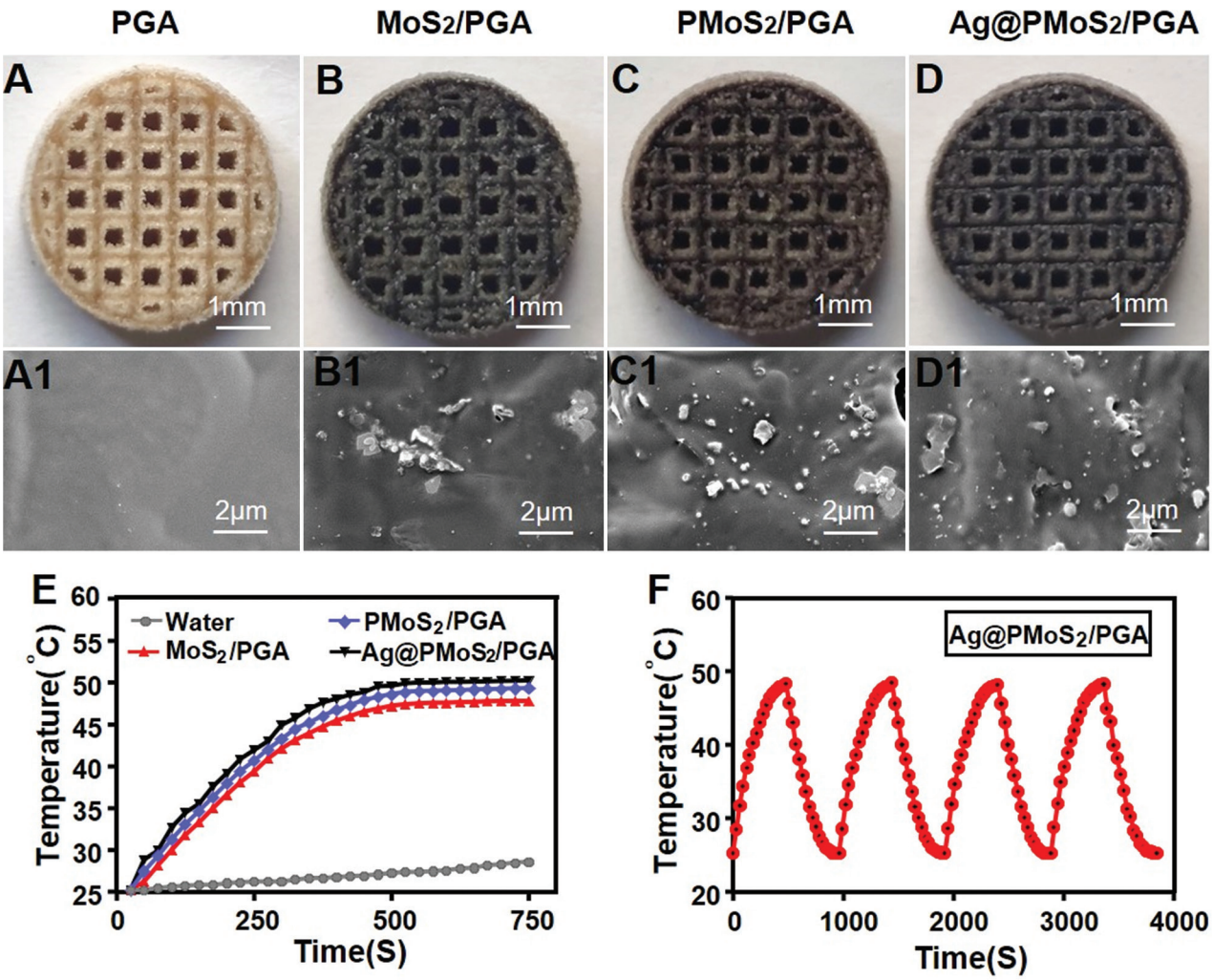

Figure 4. The microstructure and photothermal performance of scaffolds. (A-D) Photographs and (A1-D1) SEM images of the cross-section of the composite scaffolds. (E) Real-time temperature of PGA, MoS_2/PGA, $PMoS_2$/PGA, and Ag@$PMoS_2$/PGA scaffolds during NIR irradiation. (F) Real-time temperature of Ag@$PMoS_2$/PGA scaffolds under "on-off" cycles during the NIR irradiation.

In general, scaffolds suitable for cell adhesion, growth, migration, and appropriate mechanical strength should have an aperture between 100 μm and 1000 μm[40-43]. The aperture of the composite scaffolds prepared in this study was about 500 um, which was within a reasonable range. **Figure 4A1-D1** shows the SEM images of the cross section of the composite scaffolds fractured by liquid nitrogen. It is obvious that there are some aggregates from the MoS_2/PGA matrix due to the strong van der Waals forces of MoS_2 NSs[44]. Conversely, the Ag@$PMoS_2$ NSs were uniformly distributed in the PGA matrix, which benefited from the synergistic dispersion effect of the Ag NPs and MoS_2 NSs[45]. Furthermore, we verify the photothermal performance of composite scaffolds by irradiating 808 nm NIR laser. As shown in **Figure 4E**, Ag@$PMoS_2$/PGA scaffolds exhibited better photothermal performance than $PMoS_2$/PGA and MoS_2/PGA. Furthermore, photothermal stability of Ag@$PMoS_2$/PGA was examined by over four laser on/off cycles (1 W/cm^2). As shown in **Figure 4F**, there was no obvious reduction, which further indicates that the photothermal agent has excellent photostability.

3.4. Photothermal antitumor function of scaffolds

To further confirm the photothermal antitumor efficacy of composite scaffolds, MG63 cells were cultured with sterilized scaffolds and irradiated with or without 808 nm NIR for 10 min. The cells were stained with PI in red and calcein-AM in green, respectively, and the live/dead staining status was evaluated by a fluorescence microscope. The dead cells were stained in red as PI cannot enter living cells and the living cells were stained in green (calcein-AM enters dead cells and dispersed very fast and cannot be detected). As expected, both PGA, MoS_2/PGA, $PMoS_2$/PGA, and Ag@$PMoS_2$/

Please cite this article as: Zheng L, Zhong Y, He T, *et al*., 2022, A Codispersed Nanosystem of Silver-anchored MoS_2 Enhances Antibacterial and Antitumor Properties of Selective Laser Sintered Scaffolds, *Int J Bioprint*, 8(3):0025. http://doi.org/10.18063/ijb.v8i3.0025

PGA scaffolds showed no cytotoxicity without NIR irradiation (**Figure 5A** and **B**). However, under NIR laser irradiation, MoS_2/PGA, $PMoS_2$/PGA, and Ag@$PMoS_2$/PGA scaffolds significantly ablated MG63 cells. The area occupied by living cells decreased on average by 8.4%, which was significant superior to the PGA scaffolds alone (**Figure 5A** and **B**). More importantly, compared with MoS_2/PGA, the ablation effect of Ag@$PMoS_2$/PGA on tumor cells was significantly enhanced (**Figure 5A** and **B**). Cell Counting Kit-8 also showed that the survival rate of MG63 cells decreased significantly by 39% (**Figure 5C**).

3.5. Effect of photothermal function of scaffold on normal cells

At the same time, we also evaluated the effect of composite scaffolds on normal cells. BMSC cells were cultured with sterilized scaffolds and irradiated with or without 808 nm NIR for 10 min. As show in **Figure 6A**, under NIR laser irradiation, MoS_2/PGA, $PMoS_2$/PGA, and Ag@$PMoS_2$/PGA scaffolds also ablated BMSC cells. The area ratio of living cells decreased by about 2% (**Figure 6B**). However, the ablation effect of these scaffolds on MSC cells was significantly reduced compared with those on MG63 cells. As shown in **Figure 5C** and **6C**, two kinds of cells were cocultured with the composite scaffold, respectively, the activity of MG63 cells was about 0.5, while that of BMSC cells was still about 1.4 after NIR irradiation. This is because tumor cells are far less tolerant to heat than normal cells and are easily killed by high temperature. When the tumor tissue was heated at about 43°C, the permeability of tumor cell membrane was increased. When the temperature is above 50°C, the

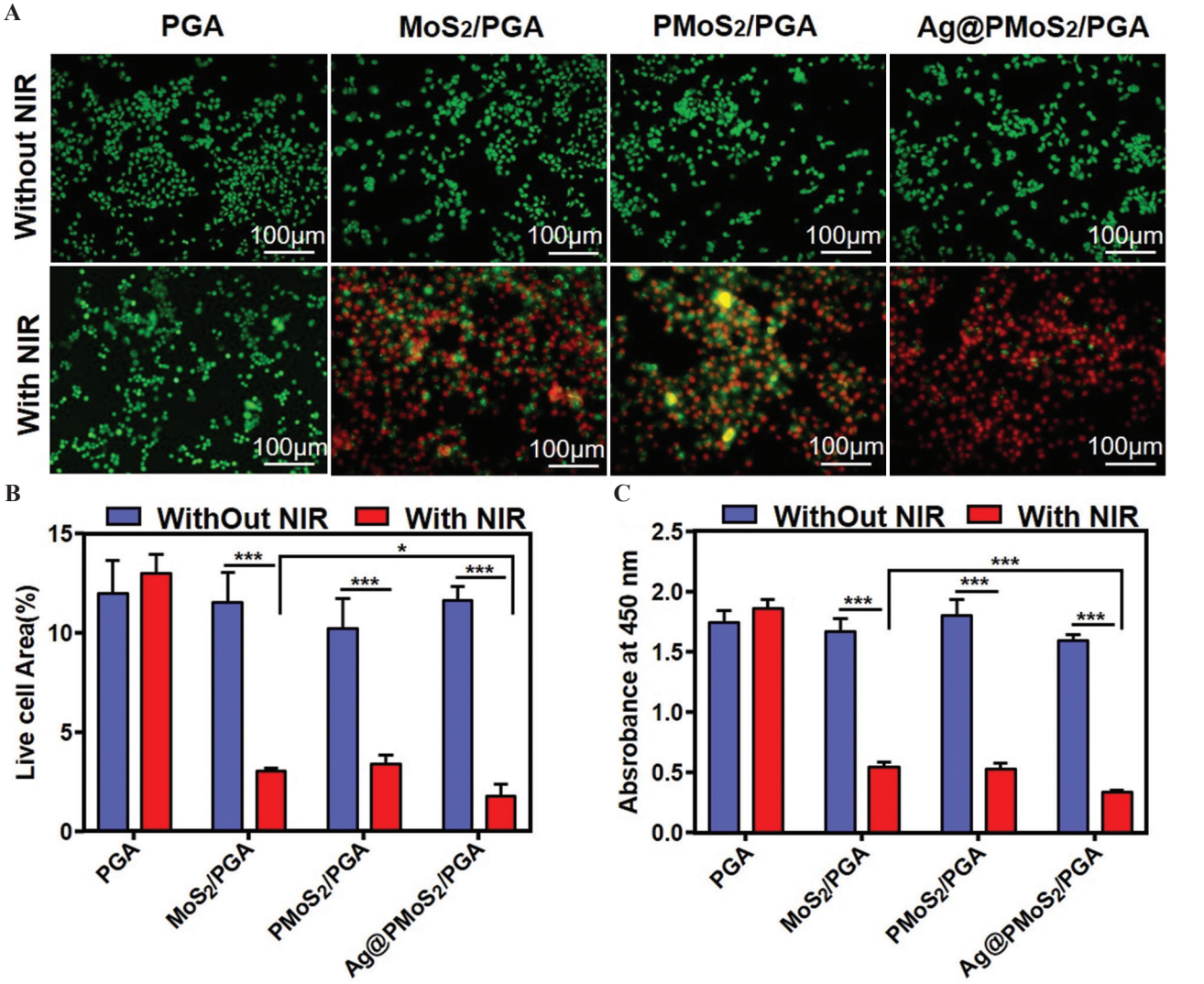

Figure 5. *In vitro* photothermal antitumor role of the composite scaffolds fabricated by SLS. Live/dead staining (A), statistical diagram of living cell proportion area (B), and Cell Counting Kit-8 assay (C) of MG63 cells after incubation with PGA, MoS_2/PGA, $PMoS_2$/PGA, and Ag@$PMoS_2$/PGA scaffolds with or without 808 nm NIR irradiation (1 W/cm^2, 10 min).

Please cite this article as: Zheng L, Zhong Y, He T, *et al*., 2022, A Codispersed Nanosystem of Silver-anchored MoS_2 Enhances Antibacterial and Antitumor Properties of Selective Laser Sintered Scaffolds, *Int J Bioprint*, 8(3):0025. http://doi.org/10.18063/ijb.v8i3.0025

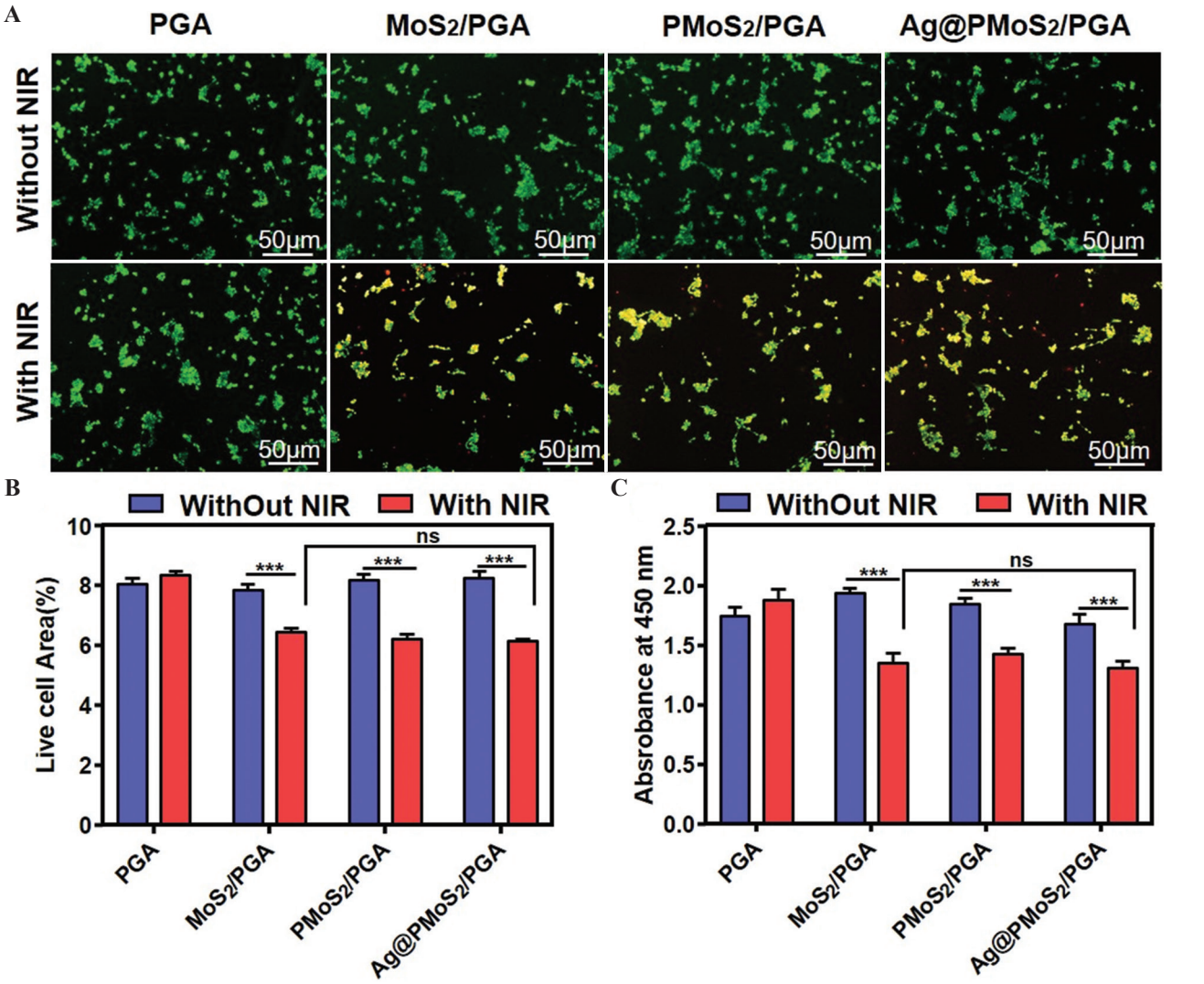

Figure 6. Photothermal effect of the scaffolds on normal cells. Live/dead staining (A), statistical diagram of living cell proportion area (B), and Cell Counting Kit-8 assay (C) of BMSC cells after incubation with PGA, MoS_2/PGA, $PMoS_2$/PGA, and Ag@$PMoS_2$/PGA scaffolds with or without 808 nm NIR irradiation (1 W/cm^2, 10 min).

thermal effect will destroy the tumor tissue, resulting in apoptosis and necrosis of tumor cells, thus achieving the purpose of treatment[46,47].

3.6. The scaffold selectively induced apoptosis *in vitro*

Above results demonstrate that the composite scaffolds can effectively cause tumor cell death under NIR irradiation. It is well known that apoptosis and necrosis are two common but completely different pathways of cell death. Some studies have shown that photothermal therapy can be used as an antitumor therapy because it can induce apoptosis and necrosis of tumor cells[48-50]. In necrosis, cell function is completely destroyed, along with the loss of membrane integrity, in which cell contents leak out of the cell uncontrollably, causing an inflammatory response[51]. In the process of apoptosis, the cell can retain the integrity of plasma membrane, and the phagocytes selectively recognize and quickly engulf the apoptotic cells[52]. Recent studies have shown that photothermal therapy at low power density can induce apoptosis rather than necrosis[53,54]. To further investigate the mode of tumor cell death induced by composite scaffolds, flow cytometry was performed. As shown in **Figure 7A**, NIR irradiation of MoS_2 samples significantly promoted the apoptosis of MG63 cells. **Figure 7B** shows the statistics of apoptosis rate, it was observed that the rate of cell apoptosis in the MoS_2 sample increased from 3.3% to 11.6% after NIR irradiation, while PGA scaffolds remained unchanged. More importantly, compared with MoS_2/PGA scaffolds, the apoptosis of MG63 cells

Please cite this article as: Zheng L, Zhong Y, He T, *et al*., 2022, A Codispersed Nanosystem of Silver-anchored MoS_2 Enhances Antibacterial and Antitumor Properties of Selective Laser Sintered Scaffolds, *Int J Bioprint*, 8(3):0025. http://doi.org/10.18063/ijb.v8i3.0025

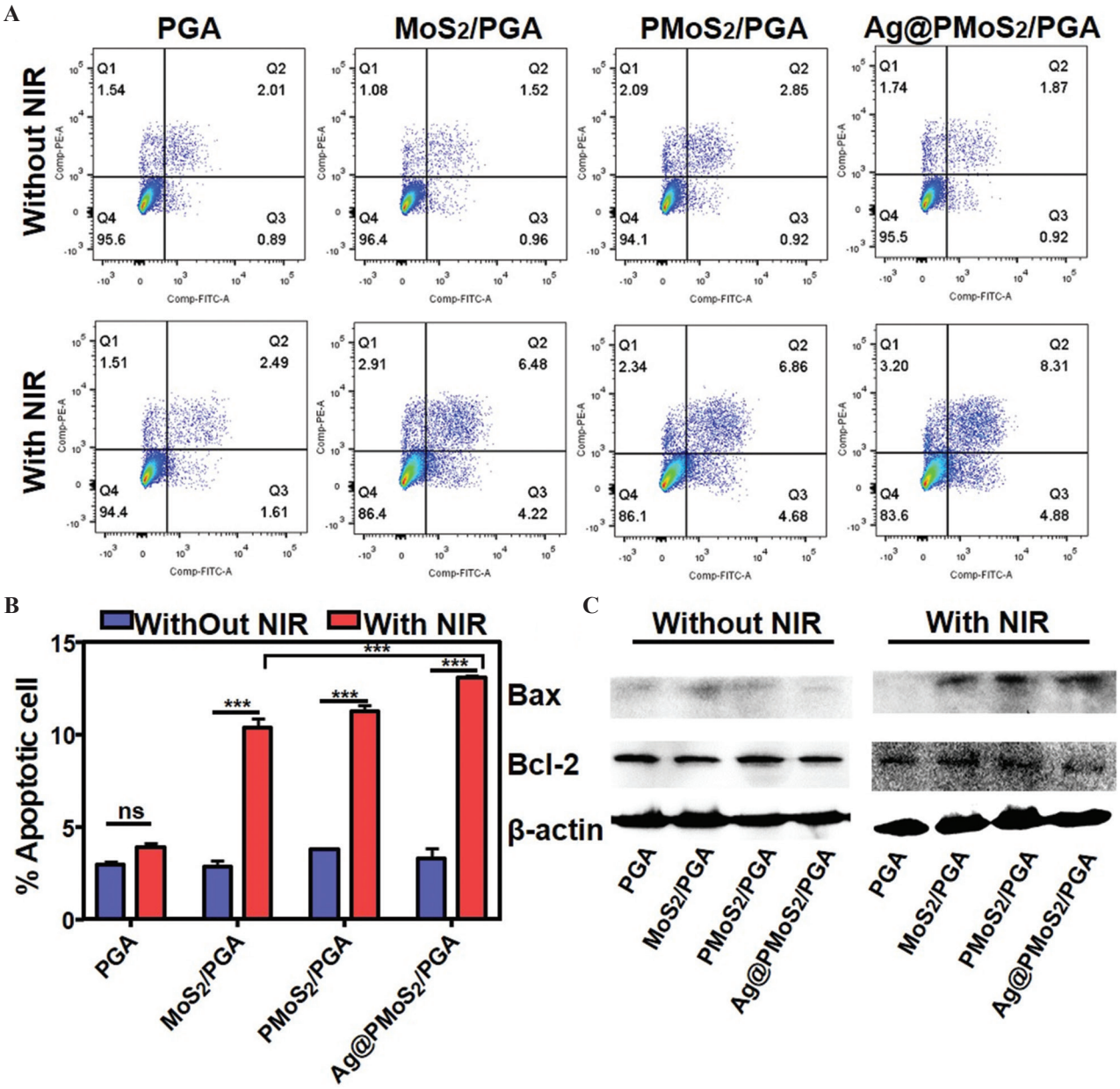

Figure 7. The scaffolds selectively induced apoptosis *in vitro*. (A) FCM (flow cytometry) for apoptosis of MG63 cells after incubation with PGA, MoS_2/PGA, $PMoS_2$/PGA, and Ag@$PMoS_2$/PGA scaffolds with or without 808 nm NIR irradiation (1 W/cm^2, 10 min). (B) Statistics analysis of the apoptosis rate. (C) Western blot analysis of Bcl-2 and Bax protein expression in MG63 cells after incubation with PGA, MoS_2/PGA, $PMoS_2$/PGA, and Ag@$PMoS_2$/PGA scaffolds with or without 808 nm NIR irradiation (1 W/cm^2, 10 min).

induced by Ag@$PMoS_2$/PGA scaffolds after NIR irradiation was significantly increased by 2.7%, which was consistent with the previous results. Bax and Bcl-2 are Bcl-2 family genes. Bax promotes apoptosis and Bcl-2 inhibits apoptosis. Western blot was performed to detect the expression of Bax and Bcl-2 proteins in cells before and after photothermal treatment. As shown in **Figure 7C**, Bax protein was increased and Bcl-2 protein expression was inhibited after photothermal treatment. Factors reported to influence photothermal therapy-induced cell death patterns include photothermal conversion efficiency and concentration of photothermal reagents, laser power density, and exposure time[55]. Here, the data showed that the scaffolds MoS_2/PGA, $PMoS_2$/PGA, and Ag@$PMoS_2$/PGA induced the apoptosis of osteosarcoma cells under NIR irradiation at low density (1 W/cm^2) for 10 min.

3.7. Antibacterial function of scaffolds

Clinically, it was well known that the bacterial infection was one problem causing orthopedic implant failure[56,57].

Please cite this article as: Zheng L, Zhong Y, He T, *et al*., 2022, A Codispersed Nanosystem of Silver-anchored MoS_2 Enhances Antibacterial and Antitumor Properties of Selective Laser Sintered Scaffolds, *Int J Bioprint*, 8(3):0025. http://doi.org/10.18063/ijb.v8i3.0025

The antibacterial ability of composite scaffold was evaluated by coculture of scaffolds and bacteria. As shown in **Figure 8A** and **B**, PGA, MoS_2/PGA, and $PMoS_2$/PGA scaffolds have very weak antibacterial activity to *E. coli* without NIR irradiation. While MoS_2/PGA and $PMoS_2$/PGA scaffolds show moderate photothermal antibacterial properties during NIR laser irradiation. Due to the powerful antibacterial properties of Ag, Ag@$PMoS_2$/PGA scaffolds have superior antibacterial properties without NIR irradiation. Moreover, the antibacterial activity of Ag@$PMoS_2$/PGA scaffolds was enhanced after NIR irradiation. The morphology of bacterial was observed by scanning electron microscope. In the absence of NIR irradiation, a large number of rod-shaped bacteria conglutinated together on the surface of the Ag-free scaffold. In contrast, the content of adherent bacteria decreased significantly in the presence of silver. More importantly, the bacteria's appearance becomes distorted and shrunken, indicating damage to their cellular structure. Compared with the scaffolds without NIR irradiation, the number of bacteria attached to the surface of MoS_2 scaffolds after NIR irradiation was lower and the morphology was more atrophied, especially the Ag@$PMoS_2$/PGA scaffolds (**Figure 8C**).

3.8. Release of silver ions by scaffold upregulated the level of ROS in bacteria

To explore the mechanism of antibacterial performance of scaffold, the release kinetics of Ag^+ of the Ag@$PMoS_2$/PGA scaffold was studied. The amount of non-cumulative Ag^+ release in deionized water is shown in **Figure 9A**. It can be observed that the release amount of Ag^+ is 0.87 μg/mL on the 1st day. With the extension of leaching time, the release amount of Ag^+ gradually decreases and tends to be stable. The cumulative release experiment showed that the Ag^+ release gradually increased with time dependence (**Figure 9B**). It was considered that the good stability of Ag NPs formed by *in situ* reduction, the lamellar structure of MoS_2 NSs, and the inclusion of polymer matrix all contribute to the slow release of Ag^+[58-61]. This sustained release property contributes to long-term antibacterial action without sacrificing its biocompatibility[62]. It has been reported that Ag or Ag^+ ions can upregulate intracellular ROS levels, resulting the destruction of cellular structure and function in many bacteria[63]. Then, we further detected the ROS level in the bacteria, and the results are shown in **Figure 9C**. It can be seen that silver-free scaffolds have no significant

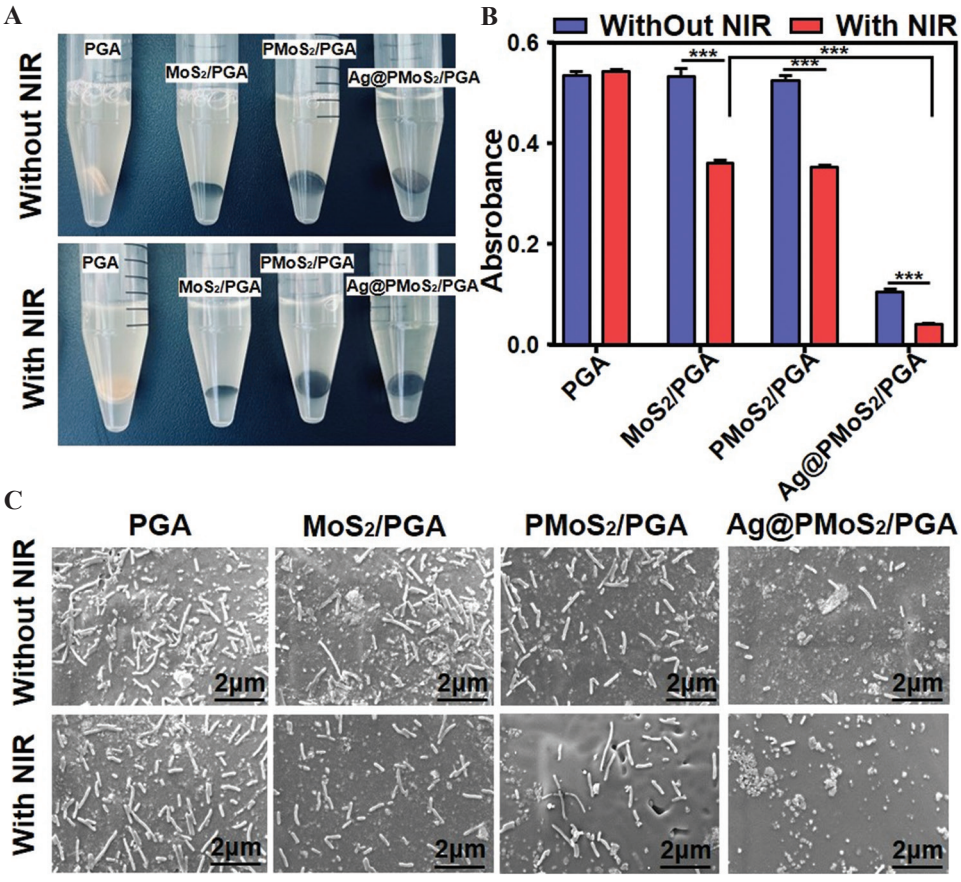

Figure 8. The scaffolds selectively inhibit the bacterial proliferation and survival. (A) The photographs of turbidity of bacterial fluid. (B) Absorption value of bacterial culture medium at 600 nm. (C) SEM of the morphologies of *Escherichia coli* on scaffolds.

Please cite this article as: Zheng L, Zhong Y, He T, *et al*., 2022, A Codispersed Nanosystem of Silver-anchored MoS_2 Enhances Antibacterial and Antitumor Properties of Selective Laser Sintered Scaffolds, *Int J Bioprint*, 8(3):0025. http://doi.org/10.18063/ijb.v8i3.0025

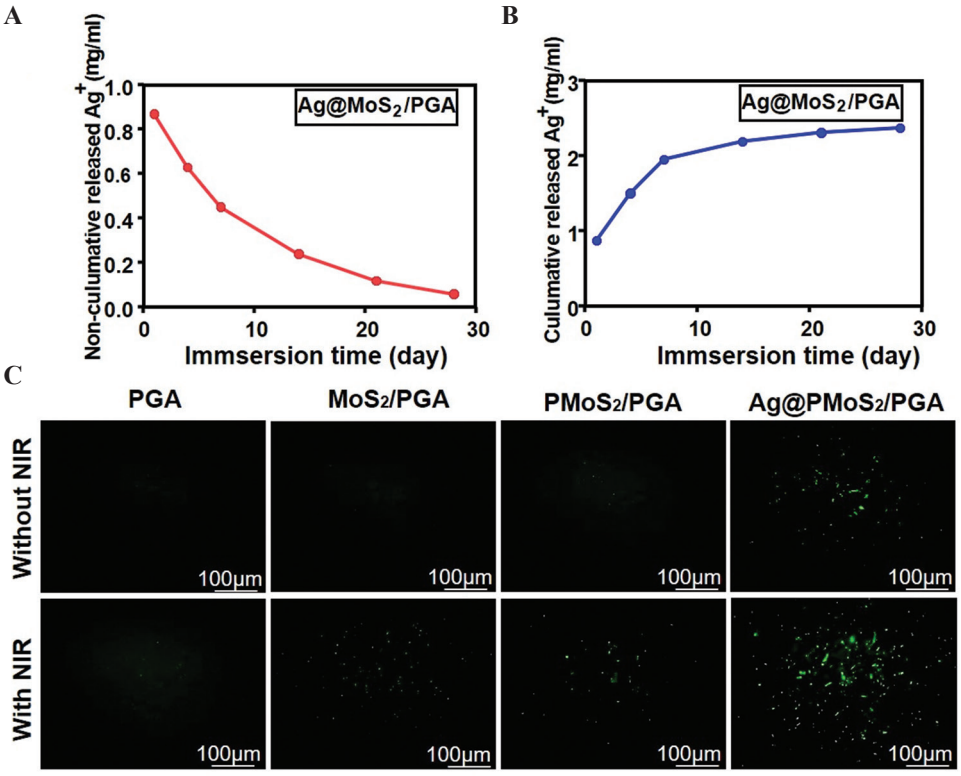

Figure 9. Release of silver ions by scaffold upregulated the level of ROS in bacteria. Non-cumulative (A) and cumulative (B) Ag^+ concentration released of Ag@PMoS$_2$/PGA scaffold. (C) Fluorescence microscope images of *Escherichia coli* incubated with DCFH-DA after incubation with PGA, MoS$_2$/PGA, PMoS$_2$/PGA, and Ag@PMoS$_2$/PGA scaffolds with or without 808 nm NIR irradiation (1 W/cm^2, 10 min).

change in ROS content in bacteria with or without NIR irradiation. While the Ag@PMoS$_2$/PGA scaffold can up-regulate the ROS level in bacteria without NIR laser. And the ROS level in bacteria was more significantly upregulated when irradiated with NIR laser.

4. Conclusion

A novel antitumor and antibacterial composite scaffold based on MoS$_2$ NSs loaded with *in situ* grown Ag NPs was designed and constructed by SLS technology. This *in situ* growth mode has a synergistic dispersion effect and helps prevent the agglomeration of Ag NPs and MoS2 NSs in the polymer scaffold. Meanwhile, MoS$_2$ NSs can provide a barrier layer for Ag^+ to react with external solution and control its stable release. The data showed that the composite scaffolds had stronger photothermal and antitumor effects and could induce tumor cell apoptosis. The scaffolds also have stronger antibacterial function through upregulation of ROS in bacteria. In conclusion, the porous Ag@PMoS$_2$/PGA composite scaffold may be a promising candidate for preventing tumor recurrence and bacterial infection in reconstruction after bone tumor surgery.

Acknowledgments

This study was supported by the National Natural Science Foundation of China (No. 51935014, 81871498, 82072084, 81871494), Jiangxi Provincial Natural Science Foundation of China (20192ACB20005), and Innovation for graduate students of Central South University 2020 (2020zzts774, 2020zzts223). Special thanks to the technical platform and experiment assistance of the Institute of Biological Additive Manufacturing of Jiangxi University of Science and Technology.

Conflict of interest

The authors declare that there are no competing interests.

Author contributions

S.P. guided and supervised the project. L.Z. designed and supervised the experiments. L.Z., Y.Z., and T.H. carried out the experiments. L.Z. interpreted data and wrote the manuscript with support from Y.Z., T.H., and L.Y.; S.P. and L.Y. mentored the technical part of the project. All authors read and approved the manuscript.

Please cite this article as: Zheng L, Zhong Y, He T, *et al*., 2022, A Codispersed Nanosystem of Silver-anchored MoS$_2$ Enhances Antibacterial and Antitumor Properties of Selective Laser Sintered Scaffolds, *Int J Bioprint*, 8(3):0025. http://doi.org/10.18063/ijb.v8i3.0025

References

1. Yang Q, Yin H, Xu T, *et al.*, 2020, Engineering 2D Mesoporous Silica@MXene-Integrated 3D-Printing Scaffolds for Combinatory Osteosarcoma Therapy and NO-Augmented Bone Regeneration. *Small*, 16:e1906814. https://doi.org/10.1002/smll.201906814
2. Smeland S, Bielack SS, Whelan J, *et al.*, 2019, Survival and Prognosis with Osteosarcoma: Outcomes in more than 2000 Patients in the EURAMOS-1 (European and American Osteosarcoma Study) cohort. *Eur J Cancer*, 109:36–50. https://doi.org/10.1016/j.ejca.2018.11.027
3. Dang W, Li T, Li B, *et al*., 2018, A Bifunctional Scaffold with CuFeSe2 Nanocrystals for Tumor Therapy and Bone Reconstruction. *Biomaterials*, 160:92–106. https://doi.org/10.1016/j.biomaterials.2017.11.020
4. Feng P, Jia J, Peng S, *et al*., 2022, Transcrystalline Growth of PLLA on Carbon Fiber Grafted with Nano-SiO_2 Towards Boosting Interfacial Bonding in Bone Scaffold. *Biomater Res*, 26:2. https://doi.org/10.1186/s40824-021-00248-0
5. Zan J, Qian G, Deng F, *et al*., 2022, Dilemma and Breakthrough of Biodegradable Poly-l-lactic Acid in Bone Tissue Repair. *J Mater Res Technol*, 2369–87. https://doi.org/10.1016/j.jmrt.2022.01.164
6. Li Y, Yang Y, Huang Z, *et al*., 2020, Bone Defect Reconstruction with Autologous Bone Inactivated with Liquid Nitrogen after Resection of Primary Limb Malignant Tumors: An Observational Study. *Medicine* (*Baltimore*), 99:e20442. https://doi.org/10.1097/MD.0000000000020442
7. Zhu C, He M, Sun D, *et al*., 2021, 3D-Printed Multifunctional Polyetheretherketone Bone Scaffold for Multimodal Treatment of Osteosarcoma and Osteomyelitis. *ACS Appl Mater Interfaces*, 13:47327–40. https://doi.org/10.1021/acsami.1c10898
8. Li K, Cai K, Ran Q, *et al*., 2019, Biomimetic Triphase Composite Scaffolds with Antibacterial and Anti-Tumor Potentials for Bone Repair. *Mater Lett*, 256:126590. https://doi.org/10.1016/j.matlet.2019.126590
9. Wang L, Yang Q, Huo M, *et al*., 2021, Engineering Single-Atomic Iron-Catalyst-Integrated 3D-Printed Bioscaffolds for Osteosarcoma Destruction with Antibacterial and Bone Defect Regeneration Bioactivity. *Adv Mater*, 33:e2100150. https://doi.org/10.1002/adma.202100150
10. He M, Zhu C, Xu H, *et al*., 2020, Conducting Polyetheretherketone Nanocomposites with an Electrophoretically Deposited Bioactive Coating for Bone Tissue Regeneration and Multimodal Therapeutic Applications. *ACS Appl Mater Interfaces,* 12(51): 56924-56934. https://doi.org/10.1021/acsami.0c20145
11. Chen SC, Lin CY, Cheng TL, *et al*., 2017, 6-Mercaptopurine-Induced Fluorescence Quenching of Monolayer MoS2 Nanodots: Applications to Glutathione Sensing, Cellular Imaging, and Glutathione-Stimulated Drug Delivery. *Adv Funct Mater*, 27:1702452. https://doi.org/10.1002/adfm.201702452
12. Gao Q, Zhang X, Yin W, *et al*., 2018, Functionalized MoS2 Nanovehicle with Near-Infrared Laser-Mediated Nitric Oxide Release and Photothermal Activities for Advanced Bacteria-Infected Wound Therapy. *Small*, 14:e1802290. https://doi.org/10.1002/smll.201802290
13. Yu J, Yin W, Zheng X, *et al*., 2015, Smart MoS2/Fe_3O_4 Nanotheranostic for Magnetically Targeted Photothermal Therapy Guided by Magnetic Resonance/Photoacoustic Imaging. *Theranostics*, 5:931–45. https://doi.org/10.7150/thno.11802
14. Cheng L, Wang X, Gong F, *et al*., 2020, 2D Nanomaterials for Cancer Theranostic Applications. *Adv Mater*, 32:e1902333. https://doi.org/10.1002/adma.201902333
15. Cai S, Yan J, Xiong H, *et al*., 2020, Aptamer-Functionalized Molybdenum Disulfide Nanosheets for Tumor Cell Targeting and Lysosomal Acidic Environment/NIR Laser Responsive Drug Delivery to Realize Synergetic Chemo-Photothermal Therapeutic Effects. *Int J Pharm*, 590:119948. https://doi.org/10.1016/j.ijpharm.2020.119948
16. Fu S, Zhang Y, Qin G, *et al*., 2021, Antibacterial Effect of TiAg Alloy Motivated by Ag-Containing Phases. *Mater Sci Eng C Mater Biol Appl*, 128:112266. https://doi.org/10.1016/j.msec.2021.112266
17. Liu A, Wang CZ, Chu C, *et al*., 2018, Adsorption Performance toward Organic Pollutants, Odour Control and Anti-Microbial Activities of One Ag-Based Coordination Polymer. 6:4961–9. https://doi.org/10.1016/j.jece.2018.07.035
18. Gao C, Yao M, Peng S, *et al*., 2021, Pre-Oxidation Induced *In Situ* Interface Strengthening in Biodegradable Zn/nano-

Please cite this article as: Zheng L, Zhong Y, He T, *et al*., 2022, A Codispersed Nanosystem of Silver-anchored MoS_2 Enhances Antibacterial and Antitumor Properties of Selective Laser Sintered Scaffolds, *Int J Bioprint*, 8(3):0025. http://doi.org/10.18063/ijb.v8i3.0025

SiC Composites Prepared by Selective Laser Melting. *J Adv Res*, 38:143–55. https://doi.org/10.1016/j.jare.2021.09.014

19. Feng P, Kong Y, Liu M, *et al*., 2021, Dispersion Strategies for Low-Dimensional Nanomaterials and Their Application in Biopolymer Implants. 100127. *Mater Today*, 2021:100127. https://doi.org/10.1016/j.mtnano.2021.100127
20. Shuai C, Guo W, Wu P, *et al*., 2018, A Graphene Oxide-Ag Co-Dispersing Nanosystem: Dual Synergistic Effects on Antibacterial Activities and Mechanical Properties of Polymer Scaffolds. *Chem Eng J*, 347:322–33. https://doi.org/10.1016/j.cej.2018.04.092
21. Yang M, Shuai Y, Yang Y, *et al*., 2022, *In situ* Grown Rare Earth Lanthanum on Carbon Nanofibre for Interfacial Reinforcement in Zn Implants. *Virtual Phys Prototyp*, 2022:1-18. https://doi.org/10.1080/17452759.2022.2053929
22. Ali I, Hussain R, Louis H, *et al*., 2021, *In situ* Reduced Graphene-Based Aerogels Embedded with Gold Nanoparticles for Real-Time Humidity Sensing And Toxic Dyes Elimination. *Mikrochim Acta*, 188:10. https://doi.org/10.1007/s00604-020-04658-0
23. Xu P, Liang J, Cao X, *et al*., 2016, Facile Synthesis of Monodisperse of Hollow Mesoporous SiO_2 Nanoparticles and *In-Situ* Growth of Ag Nanoparticles for Antibacterial. *J Colloid Interface Sci*, 474:114–8. https://doi.org/10.1016/j.jcis.2016.04.009
24. Qi F, Zeng Z, Yao J, *et al*., 2021, Constructing Core-Shell Structured $BaTiO_3$@ Carbon Boosts Piezoelectric Activity and Cell Response of Polymer Scaffolds. *Mater Sci Eng C*, 126:112129. https://doi.org/10.1016/j.msec.2021.112129
25. Hu Y, Dan W, Xiong S, *et al*., 2017, Development of Collagen/Polydopamine Complexed Matrix as Mechanically Enhanced and Highly Biocompatible Semi-Natural Tissue Engineering Scaffold. *Acta Biomater*, 47:135–48. https://doi.org/10.1016/j.actbio.2016.10.017
26. Chen T, Liu Z, Zhang K, *et al*., 2021, Mussel-Inspired Ag NPs Immobilized on Melamine Sponge for Reduction of 4-Nitrophenol, Antibacterial Applications and Its Superhydrophobic Derivative for Oil-Water Separation. *ACS Appl Mater Interfaces*, 13:50539–51. https://doi.org/10.1021/acsami.1c14544
27. Yang Y, Yang M, He C, *et al.*, 2021, Rare Earth Improves Strength and Creep Resistance of Additively Manufactured Zn Implants. *Compos Part B Eng*, 216:108882. https://doi.org/10.1016/j.compositesb.2021.108882
28. Yang Y, Lu C, Shen L, *et al*., 2021, *In-Situ* Deposition of Apatite Layer to Protect Mg-Based Composite Fabricated Via Laser Additive Manufacturing. *J Magn Alloys*, in press. https://doi.org/10.1016/j.jma.2021.04.009
29. Qian G, Zhang L, Wang G, *et al*., 2021, 3D Printed Zn-doped Mesoporous Silica-incorporated Poly-L-lactic Acid Scaffolds for Bone Repair. *Int J Bioprint*, 7:346. https://doi.org/10.18063/ijb.v7i2.346
30. Feng P, Wu P, Gao C, *et al*., 2018, A Multimaterial Scaffold with Tunable Properties: Toward Bone Tissue Repair. *Adv Sci* (*Weinh*), 5:1700817. https://doi.org/10.1002/advs.201700817
31. Qi F, Liao R, Shuai Y, *et al*., 2022, A Conductive Network Enhances Nerve Cell Response. *Addit Manuf*, 52:102694. https://doi.org/10.1016/j.addma.2022.102694
32. Qi F, Gao X, Shuai Y, *et al*., 2022, Magnetic-Driven Wireless Electrical Stimulation in a Scaffold. *Compos Part B Eng*, 237:109864. https://doi.org/10.1016/j.compositesb.2022.109864
33. Wang H, Zeng X, Pang L, *et al*., 2020, Integrative Treatment of Anti-Tumor/Bone Repair by Combination of MoS2 Nanosheets with 3D Printed Bioactive Borosilicate Glass Scaffolds. *Nanoscale*, 396:125081. https://doi.org/10.1016/j.cej.2020.125081
34. Zhang Z, Zhang J, Zhang B, *et al*., 2013, Mussel-Inspired Functionalization of Graphene for Synthesizing Ag-Polydopamine-Graphene Nanosheets as Antibacterial Materials. *Nanoscale*, 5:118–23. https://doi.org/10.1039/c2nr32092d
35. Yuwen L, Sun Y, Tan G, *et al*., 2018, MoS2@polydopamine-Ag Nanosheets with Enhanced Antibacterial Activity for Effective Treatment of *Staphylococcus aureus* Biofilms and Wound Infection. *Nanoscale*, 10:16711–20. https://doi.org/10.1039/c8nr04111c
36. Xie Y, Yan B, Xu H, *et al*., 2014, Highly Regenerable Mussel-Inspired Fe(3)O(4)@polydopamine- Ag Core-Shell Microspheres as Catalyst and Adsorbent for Methylene Blue Removal. *ACS Appl Mater Interfaces*, 6:8845–52. https://doi.org/10.1021/am501632f
37. Shuai C, Xu Y, Feng P, *et al*., 2019, Antibacterial Polymer Scaffold Based on Mesoporous Bioactive Glass Loaded with *In Situ* Grown Silver. *Chem Eng J*, 374:304–15. https://doi.org/10.1016/j.cej.2019.03.273

Please cite this article as: Zheng L, Zhong Y, He T, *et al*., 2022, A Codispersed Nanosystem of Silver-anchored MoS_2 Enhances Antibacterial and Antitumor Properties of Selective Laser Sintered Scaffolds, *Int J Bioprint*, 8(3):0025. http://doi.org/10.18063/ijb.v8i3.0025

38. Shuai C, Liu G, Yang Y, *et al*., 2020, A Strawberry-Like Ag-Decorated Barium Titanate Enhances Piezoelectric and Antibacterial Activities of Polymer Scaffold. *Nano Energy*, 74:104825. https://doi.org/10.1016/j.nanoen.2020.104825
39. Zeng G, Huang L, Huang Q, *et al*., 2018, Rapid Synthesis of MoS2-PDA-Ag Nanocomposites as Heterogeneous Catalysts and Antimicrobial Agents via Microwave Irradiation. *Appl Surf Sci*, 459:588–95. https://doi.org/10.1016/j.apsusc.2018.07.144
40. Loh QL, Choong C, 2013, Three-Dimensional Scaffolds for Tissue Engineering Applications: Role of Porosity and Pore Size. *Tissue Eng Part B Rev*, 19:485–502. https://doi.org/10.1089/ten.TEB.2012.0437
41. Wang C, Shuai Y, Yang Y, *et al*., 2022, Amorphous Magnesium Alloy with High Corrosion Resistance Fabricated by Laser Powder Bed Fusion. *J Alloys Compd*, 897:163247. https://doi.org/10.1016/j.jallcom.2021.163247
42. Yang Y, Cheng Y, Yang M, *et al*., 2022, Semicoherent Strengthens Graphene/Zinc Scaffolds. *Mater Today Nano*, 17:100163. https://doi.org/10.1016/j.mtnano.2021.100163
43. Shuai C, Yu L, Feng P, *et al*., 2022, Construction of a Stereocomplex between Poly(D-lactide) Grafted Hydroxyapatite and Poly(L-lactide): Toward a Bioactive Composite Scaffold with Enhanced Interfacial Bonding. *J Mater Chem B*, 10:214–23. https://doi.org/10.1039/d1tb02111g
44. Zeng J, Xu L, Luo X, *et al*., 2021, A Novel Design of SiH/CeO_2(111) Van Der Waals Type-II Heterojunction for Water Splitting. *Phys Chem Chem Phys*, 23:2812–8. https://doi.org/10.1039/d0cp05238h
45. Feng P, Kong Y, Yu L, *et al*., 2019, Molybdenum Disulfide Nanosheets Embedded with Nanodiamond Particles: Co-Dispersion Nanostructures as Reinforcements for Polymer Scaffolds. *Appl Mater Today*, 17:216–26. https://doi.org/10.1016/j.apmt.2019.08.005
46. Wu S, Butt HJ, 2016, Near-Infrared-Sensitive Materials Based on Upconverting Nanoparticles. *Adv Mater*, 28:1208–26. https://doi.org/10.1002/adma.201502843
47. Tian B, Wang C, Zhang S, *et al*., 2011, Photothermally Enhanced Photodynamic Therapy Delivered by Nano-Graphene Oxide. *ACS Nano*, 5:7000–9. https://doi.org/10.1021/nn201560b
48. Rengan AK, Bukhari AB, Pradhan A, *et al*., 2015, *In Vivo* Analysis of Biodegradable Liposome Gold Nanoparticles as Efficient Agents for Photothermal Therapy of Cancer. *Nano Lett*, 15:842–8. https://doi.org/10.1021/nl5045378
49. Tong L, Zhao Y, Huff TB, *et al*., 2007, Gold Nanorods Mediate Tumor Cell Death by Compromising Membrane Integrity. *Adv Mater*, 19:3136–41. https://doi.org/10.1002/adma.200701974
50. Xing Y, Kang T, Luo X, *et al*., 2019, Coral-shaped Au Nanostructures for Selective Apoptosis Induction during Photothermal Therapy. *J Mater Chem B*, 7:6224–6231. https://doi.org/10.1039/c9tb01503e
51. D'Arcy MS, 2019, Cell Death: A Review of the Major Forms of Apoptosis, Necrosis and Autophagy. *Cell Biol Int*, 43:582–92. https://doi.org/10.1002/cbin.11137
52. Ndoye A, Weeraratna AT, 2016, Autophagy an emerging Target for Melanoma Therapy. *F1000Res*, 5:F1000 Faculty Rev-1888. https://doi.org/10.12688/f1000research.8347.1
53. Pan L, Liu J, Shi J, 2017, Nuclear-Targeting Gold Nanorods for Extremely Low NIR Activated Photothermal Therapy. *ACS Appl Mater Interfaces*, 9:15952–61. https://doi.org/10.1021/acsami.7b03017
54. Melamed JR, Edelstein RS, Day ES, 2015, Elucidating the Fundamental Mechanisms of Cell Death Triggered by Photothermal Therapy. *ACS Nano*, 9:6–11. https://doi.org/10.1021/acsnano.5b00021
55. Aioub M, El-Sayed MA, 2016, A Real-Time Surface Enhanced Raman Spectroscopy Study of Plasmonic Photothermal Cell Death Using Targeted Gold Nanoparticles. *J Am Chem Soc*, 138:1258–64. https://doi.org/10.1021/jacs.5b10997
56. Banin E, Hughes D, Kuipers OP, 2017, Editorial: Bacterial Pathogens, Antibiotics and Antibiotic Resistance. *FEMS Microbiol Rev*, 41:450–2. https://doi.org/10.1093/femsre/fux016
57. Yu L, He T, Yao J, *et al*., 2022, Cu Ions and Cetyltrimethylammonium Bromide Loaded Into Montmorillonite: A Synergistic Antibacterial System for Bone Scaffolds. *Mater Chem Front*, 6:103–16. https://doi.org/10.1039/D1QM01278A
58. Liu J, He K, Wu W, *et al*., 2017, *In Situ* Synthesis of Highly Dispersed and Ultrafine Metal Nanoparticles from Chalcogels. *J Am Chem Soc*, 139:2900–3. https://doi.org/10.1021/jacs.6b13279
59. Li YT, Lin SB, Chen LC, *et al*., 2017, Antimicrobial Activity

Please cite this article as: Zheng L, Zhong Y, He T, *et al*., 2022, A Codispersed Nanosystem of Silver-anchored MoS_2 Enhances Antibacterial and Antitumor Properties of Selective Laser Sintered Scaffolds, *Int J Bioprint*, 8(3):0025. http://doi.org/10.18063/ijb.v8i3.0025

and Controlled Release of Nanosilvers in Bacterial Cellulose Composites Films Incorporated with Montmorillonites. *Cellulose*, 24:4871–83.
https://doi.org/10.1007/s10570-017-1487-3

60. Qi F, Wang Z, Shuai Y, *et al*., 2022, Sr^{2+} Sustained Release System Augments Bioactivity of Polymer Scaffold. *ACS Appl Polym Mater*, 4:2691–702.
https://doi.org/10.1021/acsapm.2c00024

61. Deng F, Wu P, Qian G, *et al*., 2022, Silver-Decorated Black Phosphorus: A Synergistic Antibacterial Strategy. *Nanotechnology*, 33(24): 245708.
https://doi.org/10.1088/1361-6528/ac5aee

62. Sukhorukova IV, Sheveyko AN, Shvindina NV, *et al*., 2017, Approaches for Controlled Ag(+) Ion Release: Influence of Surface Topography, Roughness, and Bactericide Content. *ACS Appl Mater Interfaces*, 9:4259–71.
https://doi.org/10.1021/acsami.6b15096

63. Su HL, Chou CC, Hung DJ, *et al*., 2009, The Disruption of Bacterial Membrane Integrity Through ROS Generation Induced by Nanohybrids of Silver and Clay. *Biomaterials*, 30:5979–87.
https://doi.org/10.1016/j.biomaterials.2009.07.030

Publisher's note

Please cite this article as: Zheng L, Zhong Y, He T, *et al*., 2022, A Codispersed Nanosystem of Silver-anchored MoS_2 Enhances Antibacterial and Antitumor Properties of Selective Laser Sintered Scaffolds, *Int J Bioprint*, 8(3):0025. http://doi.org/10.18063/ijb.v8i3.0025